Supporting Information

Light-Driven Overall Water Splitting Enabled by a Photo-Dember Effect Realized on 3D Plasmonic Structures

Min Chen,[1] Jiajun Gu,[1,*] Cheng Sun,[1] Yixin Zhao,[2] Ruoxi Zhang,[1] Xinyuan You,[3] Qinglei Liu,[1] Wang Zhang,[1] Yishi Su,[1] Huilan Su[1] & Di Zhang[1,*]

1. *State Key Laboratory of Metal Matrix Composites, Shanghai Jiao Tong University, Shanghai 200240, China*
2. *School of Environmental Science and Engineering, Shanghai Jiao Tong University, Shanghai 200240, China*
3. *Zhiyuan College, Shanghai Jiao Tong University, Shanghai Jiao Tong University, Shanghai 200240, China*

*Correspondence and requests for materials should be addressed to J. J. G (gujiajun@sjtu.edu.cn) and D. Z. (zhangdi@sjtu.edu.cn)

Contents

Detailed Descriptions of the Photo-Dember Effect on Silver (Figure. S1).

- *Model*

The photo-Dember effect on semiconductors has been well described in many excellent literatures.[1,2] However, there are two key differences from previous works once metals are to be considered:

1) Although Boltzmann distribution can be applied to describe the carriers in non-degenerate semiconductors, we must use Fermi-Dirac distribution to treat the electrons in metals. This means that the carriers with energy lower than ε_F have no contribution to transport processes according to the Pauli exclusion principle.

2) Unlike electron/hole pairs (excitons) excited by photons in semiconductors, the main photo-generated carriers in plasmonic metals (Ag, Au, and Cu) are electrons. This is determined by the Fermi surface shape (*i.e.*, the famous "dog-bone") of these face-centered cubic (*fcc*) metals.[3] Considering the sign of effective mass, the density ratio of "electrons" to "holes" in these metals can be roughly estimated by the surface area ratio of the so called "bellies" to "necks" near the Fermi level (ε_F). This ratio is especially large in Ag, meaning that Ag can be treated similar to alkali metals as a one-band metal.[3] This is experimentally confirmed through Hall coefficient measurements, which indicates that the carriers in Ag is electron-like with a density of ~7.0×10^{28} m^{-3},[3] close to the theoretical value of 5.83×10^{28} m^{-3}.

We adopted a Drude model improved by A. Sommerfeld to simulate the dynamical distribution of photo-induced electrons in Ag. This model treats a metal as positively charged ions plus free electrons to which Fermi-Dirac distribution is applied,[3] The Ag slab is provided in Figure 1d in the main text. A series of 475 nm radiation with various irradiances are casted on its left edge. If we omit the electric current in *y* and *z* directions, the photocarrier diffusion equation[1,2] and the potential equation[1] can thus be reduced into one-dimensional (1D) expressions as

$$\frac{\partial n_e(t,x_i)}{\partial t} = I_{x=0} - \frac{n_e(t,x_i)}{\tau} + D_e \frac{\partial^2 n_e(t,x_i)}{\partial x^2} + \sigma \frac{\partial^2 W_e(t)}{\partial x^2} \quad (1)$$

$$W_e(t) = \sum_{i \neq j} \frac{\left[n_e(t,x_j) + n'(t-\Delta t) - n_0 \right] \left[n_e(t,x_i) + n'(t-\Delta t) - n_0 \right] e^2}{4\pi\varepsilon_0 r_{ij}} \quad (2)$$

where $I_{x=0}$ represents the photoelectron generation induced by the light, $n_e(t, x_i)$ is the electron density at time t and position x_i, n_0 denotes the density of free electrons in Ag (5.83×10^{28} m^{-3}), $W_e(t)$ is the potential energy at time t for which Coulomb interaction between different positions is considered, e is the electron charge, ε_0 is the vacuum permittivity, σ is the electrical conductivity of Ag (6.3×10^7 S m^{-1}), τ represents the lifetime of photo-excited electrons (10^{-13} s to 10^{-15} s,[4] we chose the most negative value of 10^{-15} s), and D_e denotes diffusion coefficient, which is further linked to σ *via* a modified Einstein relation for metals:[5]

$$D_e = \frac{2}{3} \frac{\varepsilon_F}{e^2 n_0} \sigma \quad . \quad (3)$$

In addition, $n'(t\text{-}\Delta t)$ is the density of the un-excited electrons, which can be described as

$$n'(t-\Delta t) = n_0 - \frac{1}{L} \int_l n_e(x, t-\Delta t) dx \quad . \quad (4)$$

This value increases with t but should not exceed the maximum density that can be generated by the 475 nm radiation (see the blue broken line in the inset of Figure 1c in the main text).

The first two terms on the left side of the Eq. (1) represent the generation and annihilation of photoelectrons, while the third and the fourth terms denote the diffusion and drifting current, respectively. During the calculation, the slab is evenly separated into 50 sectors in x direction and the time step Δt is set to be 10^{-16} s. The sign of charges at a certain position and time can be determined by $n_e(t, x_i) + n'(t\text{-}\Delta t) - n_0$.

- *Results*

The calculation results (Figure 1b in the main text) show that if the irradiance is comparable to that of the 475 nm component in sunlight (*i.e.*, I_0~50 W m^{-2}, within 475±10 nm), the photo-Dember voltage will be quite low. In comparison, when the irradiance increases 100- and 500-fold, the photo-Dember voltages of 37.6 mV and 141.1 mV can be

produced, respectively. Time resolved distribution of electron density caused by 100 I_0 illumination is provided in Figure 1c. The inset shows the boundaries between excited and un-excited electrons at different time. These values were calculated from $n'(t\text{-}\Delta t)$, which can be related to the electron wavevector (k) by $n'/n_0=k/k_F$, with k_F the Fermi wavevector. When the time increases, the boundaries keep on approaching the inner core (blue broken line, see Figure 1c) within which electrons cannot be excited by the 475 nm radiation. This process could achieve a quasi-static state after 10^{-12} s. Moreover, the photo-Dember voltage decreases with the slab length (Figure S1). This means that if the same photo-Dember voltage is to be achieved on a shorter structure, even stronger illumination should be applied to generate more hot electrons. Thus, an asymmetric 3D plasmnoic structure with a long period (~1.5 μm) replicated from butterfly wing scales will be a good choice to exhibit this effect.

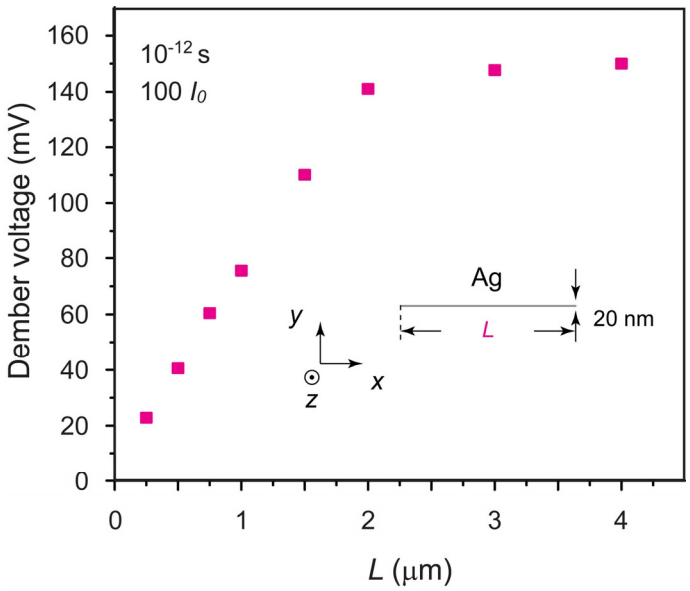

Figure S1. Photo-Dember voltages on the Ag slabs with different lengths.

Composition of Various Systems (Tables S1-S3).

Table S1. Composition of the composites for the EFM mappings and water splitting measurements (static mode).

materials	Ag [mg]	chitin [mg]	AgCl [mg]	SiO_2 [mg]
intact 3D-Ag/ AgCl	27.8(±2.7)	4.6(±1.4)	66.9(±4.3)	-
as-crushed3D-Ag/AgCl	25.5(±1.3)	4.8(±1.5)	59.5(±5.3)	-
intact 3D-Ag/ SiO_2	26.5(±2.2)	4.5(±1.2)	-	45.3(±2.4)
as-crushed3D-Ag / SiO_2	26.0(±0.9)	4.4(±1.0)	-	49.8(±3.1)

Table S2. Composition of the composites for the water splitting measurements (collision mode).

materials	Ag [mg]	chitin [mg]	AgCl [mg]	CeO_2 [mg]	WO_3 [mg]	ZnO [mg]	P25 [mg]
intact 3D-Ag+AgCl	21.2(±4.8)	3.7(±1.1)	70.1(±6.3)	-	-	-	-
as-crushed 3D-Ag+AgCl	23.2(±3.8)	4.5(±1.7)	64.4(±6.6)	-	-	-	-
intact 3D-Ag+CeO_2	21.1(±2.3)	3.8(±1.1)	-	65.0	-	-	-
as-crushed 3D-Ag+CeO_2	24.7(±3.8)	4.5(±1.3)	-	65.0	-	-	-
intact 3D-Ag+WO_3	22.2(±3.5)	3.9(±1.1)	-	-	65.0	-	-
as-crushed 3D-Ag+WO_3	25.7(±3.6)	4.5(±1.2)	-	-	65.0	-	-
intact 3D-Ag+ZnO	23.7(±3.2)	4.2(±1.2)	-	-	-	65.0	-
as-crushed 3D-Ag+ZnO	24.5(±3.5)	3.9(±1.6)	-	-	-	65.0	-
intact 3D-Ag+P25	23.8(±3.3)	4.4(±1.5)	-	-	-	-	65.0
as-crushed 3D-Ag+P25	24.7(±3.7)	4.1(±1.3)	-	-	-	-	65.0

Table S3. Composition of various systems for the evaluation of the chitin effect.

materials	Ag [mg]	chitin [mg]	AgCl [mg]	CeO_2 [mg]	WO_3 [mg]	ZnO [mg]	P25 [mg]
Ag/AgCl+chitin	23.3(±1.8)	4.0	65.0	-	-	-	-
Ag/AgCl	23.0(±1.5)	-	65.0	-	-	-	-
Ag/CeO_2+chitin	22.3(±1.0)	4.0	-	65.0	-	-	-
Ag/CeO_2	24.8(±1.5)	-	-	65.0	-	-	-
Ag/WO_3+chitin	25.0(±2.0)	4.0	-	-	65.0	-	-
Ag/WO_3	23.6(±1.8)	-	-	-	65.0	-	-
Ag/ZnO+chitin	24.2(±1.7)	4.0	-	-	-	65.0	-
Ag/ZnO	23.8(±1.4)	-	-	-	-	65.0	-
Ag/P25+chitin	24.5(±1.1)	4.0	-	-	-	-	65.0
Ag/P25	23.8(±1.6)	-	-	-	-	-	65.0

Original and the Ag-Deposited Butterfly Wings (Figure S2).

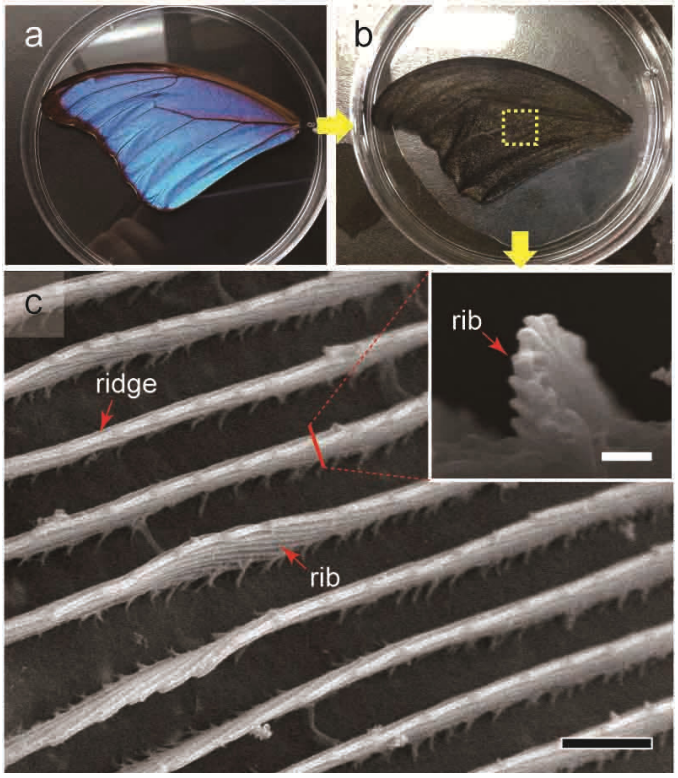

Figure S2. Photos of (a) original and (b) Ag-deposited wing of *M. didius*. (c) SEM image of a silver scale on (b). Scale bar: 2 μm. Inset shows its cross section. Scale bar: 500 nm.

Absorbance Spectra of the Original Butterfly Wing and the 3D-Ag (Figure S3).

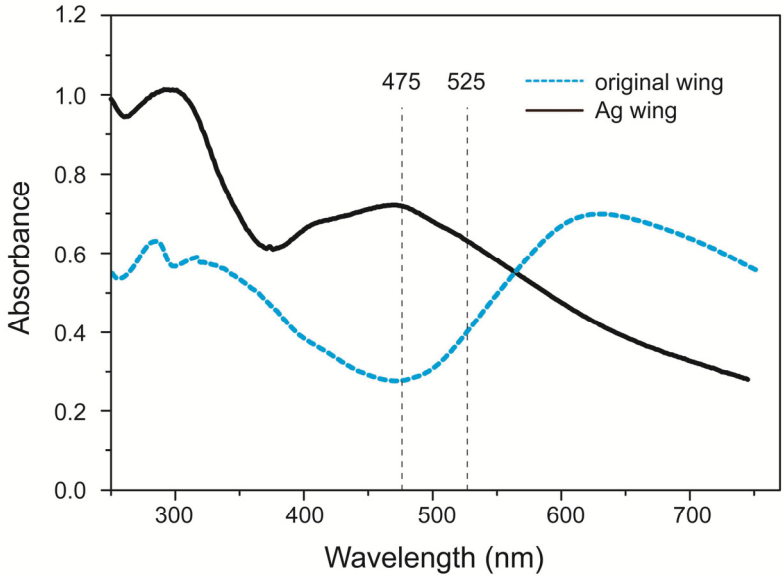

Figure S3. UV-Vis absorption spectra of an original butterfly wing (broken line) and the 3D-Ag (solid line). A surface plasmon resonance was achieved on the 3D-Ag under 475 nm irradiation.

FEM Simulation of the Hotspots Induced by the Oblique 475-nm-Irradiation on the 3D-Ag (Figure S4).

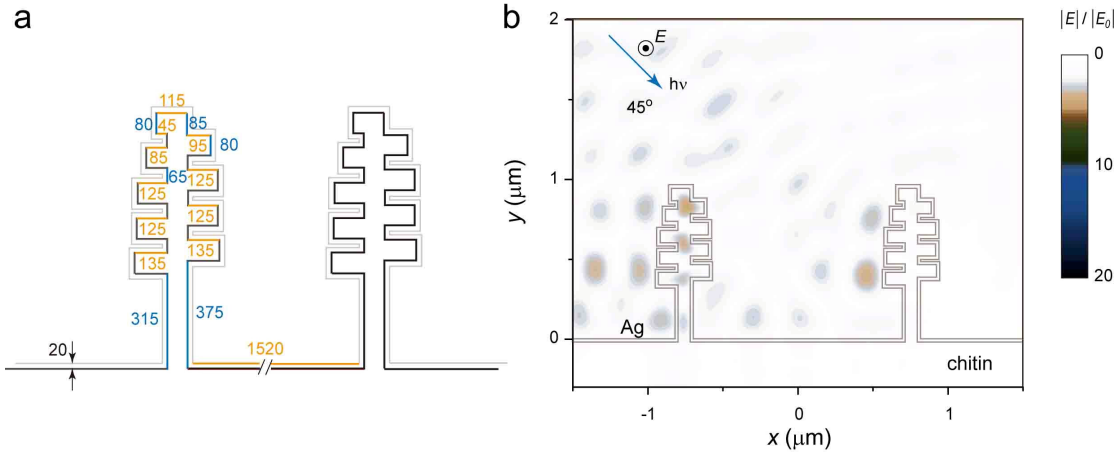

Figure S4. Two-dimensional (2D) finite element method (FEM) simulation (in air) of the electromagnetic field (EMF) distribution on the 3D-Ag excited by the 475 nm irradiation. (a) Geometric dimensions (in nanometers) of the model.[6] (b) EMF distribution under the irradiation with a transverse electric (TE) mode. The result in a transverse magnetic (TM) mode is provided in Figure 1F in the main text. Compared to the TM mode, hotspots can hardly be found in the TE mode. This is because the electric fields that drive the electrons to oscillate are out of plane here.

EFM Mappings on the 3D-Ag (Figure S5)

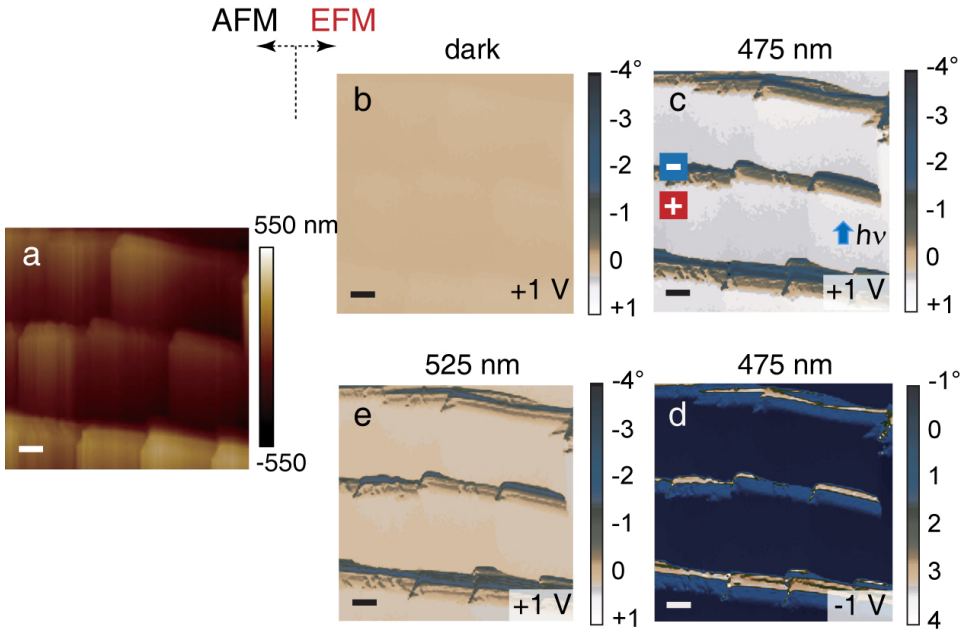

Figure S5. EFM mappings on the 3D-Ag. (a) AFM mapping; (b)-(e) EFM analyses on (a) that were conducted in the dark (b), under 475 nm irradiation with a tip bias of 1 V (c) and -1 V (d), and under 525 nm irradiation (e), respectively. Note that the sequence of (b)-(e) may be interchanged and similar phenomena are still observed. A solar simulator was used as the light source from which irradiation at a single wavelength was achieved via band-pass filters (±10 nm in wavelength). The incidence angle of illumination was 45° against the paper surface, and its projection is denoted in (c). The irradiance was 55.4 W m^{-2} and 57.8 W m^{-2} for irradiation at 475 nm and 525 nm, respectively. Scale bars: 300 nm.

EFM Mappings on the SiO_2 Particles Deposited on Structureless Ag Films (Figure S6).

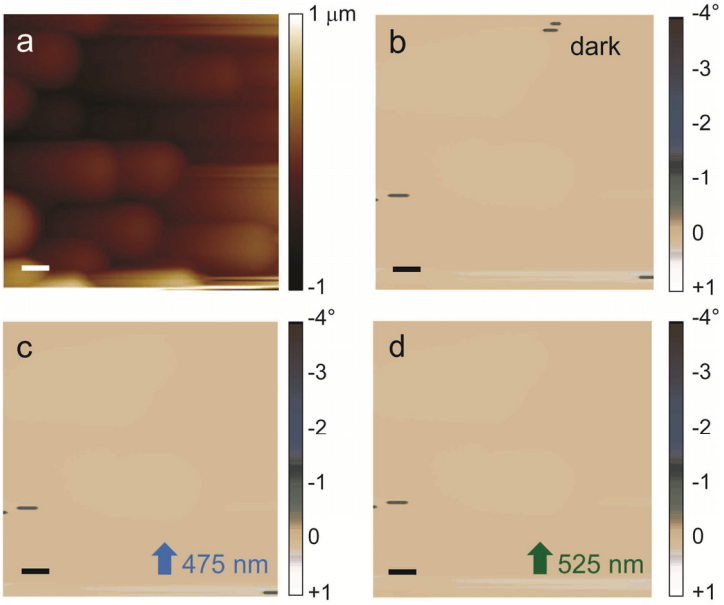

Figure S6. Surface charge distribution on a structureless Ag film with commercial SiO_2 particles deposited upon. (a) AFM scanning. (b)-(d) Corresponding electric force microscopy (EFM) mappings, which were conducted in the dark (b) and under the irradiation of 475 nm (c) and 525 nm (d), respectively. The tip bias was set to be 1 V. Compared to Figure S5 (b)-(e), no electric polarization was observed here. Scale bars: 300 nm.

FEM Simulations of the Hotspots Induced by the Oblique 475-nm-Irradiation on the 3D-Ag/SiO_2 (Figure S7).

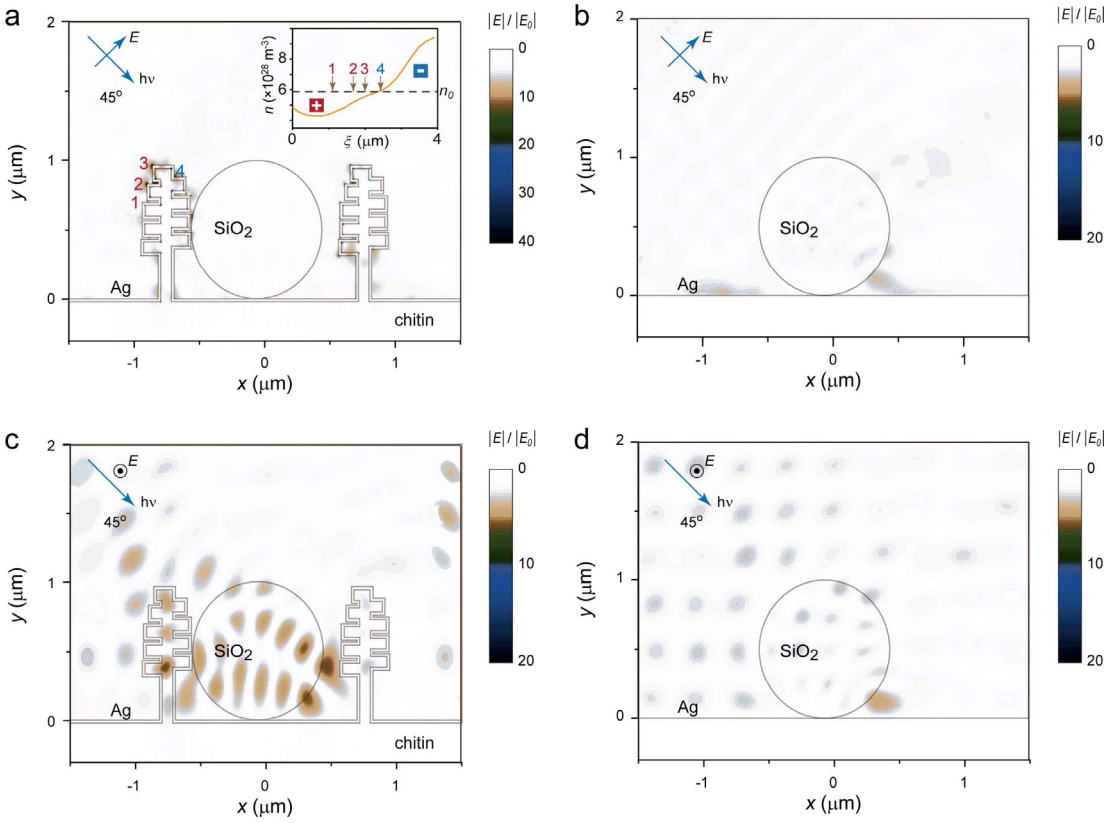

Figure S7. 2D FEM simulations (in air) of the EMF distribution on the 3D-Ag/SiO_2 excited by the 475 nm irradiation with (a), (b) TM mode and (c), (d) TE mode, respectively. The diameter of SiO_2 particle was 1 μm. Oblique irradiation was applied here and the medium was air. Hotspots with EMF enhancement over 40-fold in intensity are marked with numbers in (a). Inset in (a) shows the electron density distribution on the ridge surface.

SEM Image of the Homemade AgCl Particles (Figure S8).

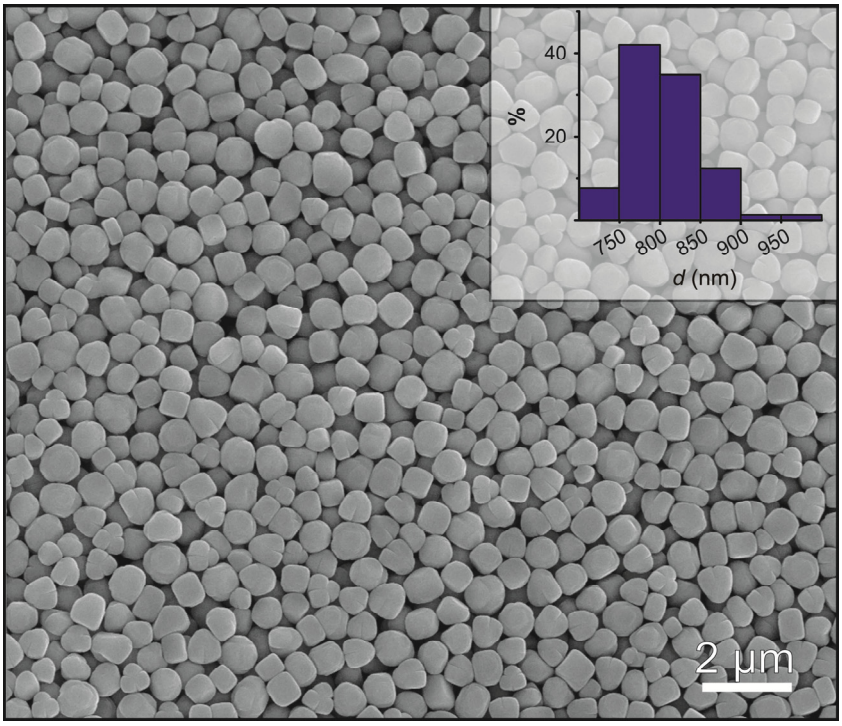

Figure S8. SEM image of the homemade AgCl particles. Inset shows the statistical diameter distribution of the AgCl particles, which mainly (over 75% in number) ranges from 750 nm to 850 nm.

Absorbance Spectra of the 3D-Ag/AgCl (Figure S9).

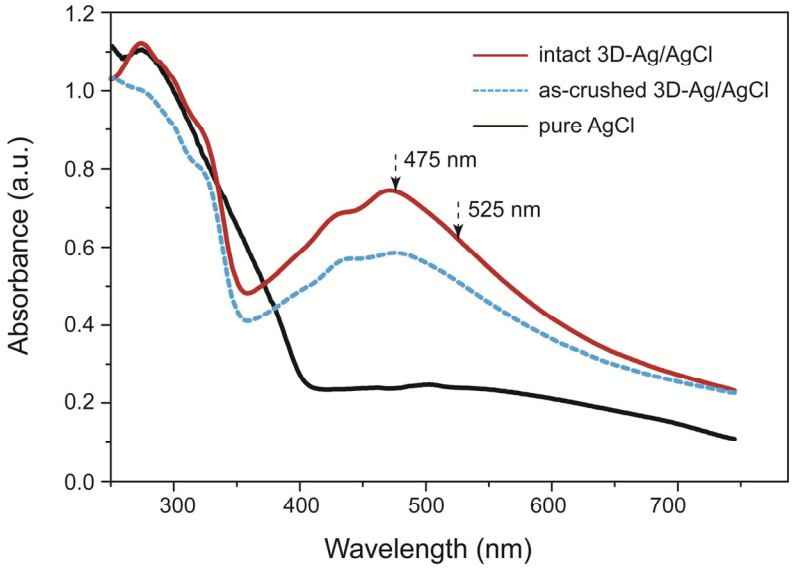

Figure S9. UV-Vis absorption spectra of the intact and as-crushed 3D-Ag/AgCl. The spectrum of pure AgCl powder is also provided for comparison.

FEM Simulations of the Hotspots Induced by the Oblique 475-nm-Irradiation on the 3D-Ag/AgCl (Figure S10).

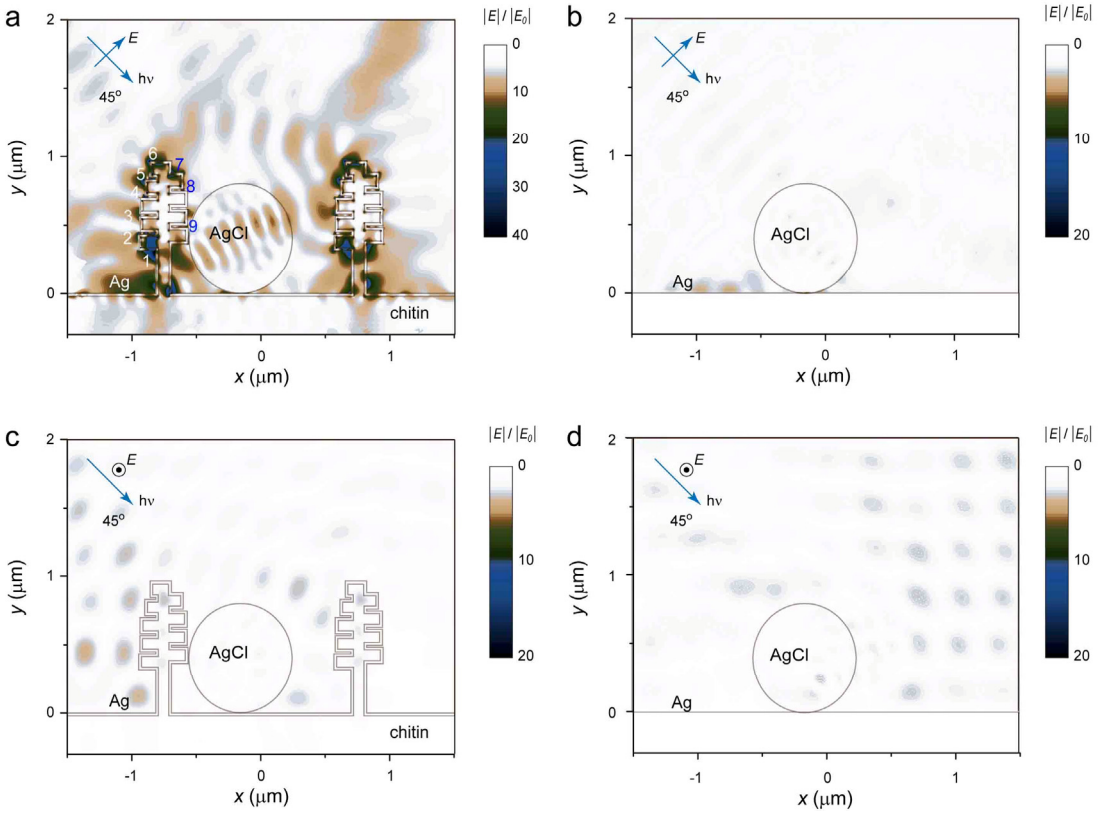

Figure S10. 2D FEM simulations (in air) of the EMF distribution on the 3D-Ag/AgCl excited by the 475 nm irradiation with (a), (b) TM mode and (c), (d) TE mode, respectively. The diameter of the AgCl particle was 800 nm. Oblique irradiation was applied here and the medium was air. Hotspots with EMF enhancement over 40-fold in intensity are marked with numbers in (a).

FEM Simulations of the Hotspots Induced by the Normal 475-nm-Irradiation on the 3D-Ag/AgCl (Figures S11, S12).

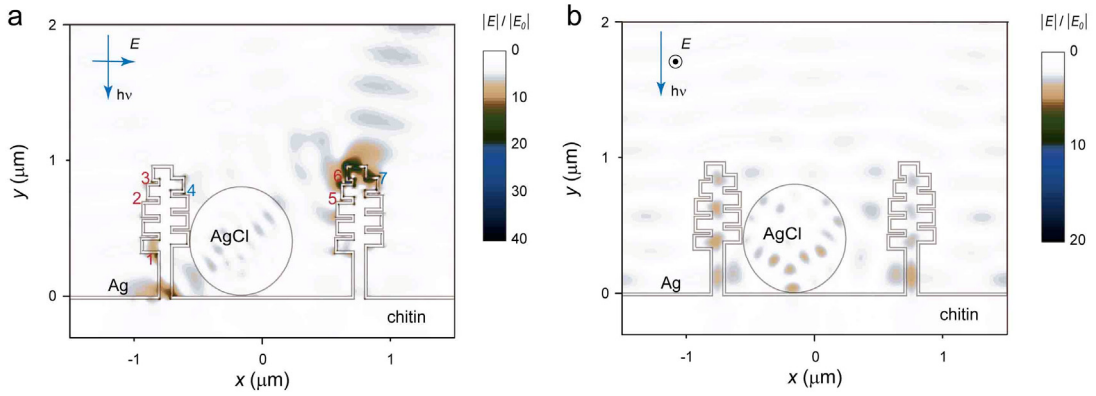

Figure S11. 2D FEM simulations (in air) of the EMF distribution on the 3D-Ag/AgCl excited by the 475 nm irradiation of (a) TM mode and (b) TE mode, respectively. The diameter of AgCl particle was 800 nm. The medium was air and normal irradiation of 475 nm was applied. Hotspots with EMF enhancement over 40-fold in intensity are marked with numbers in (a). Asymmetric spatial distribution of hotspots can be found due to the asymmetric nature of the Ag skeleton.

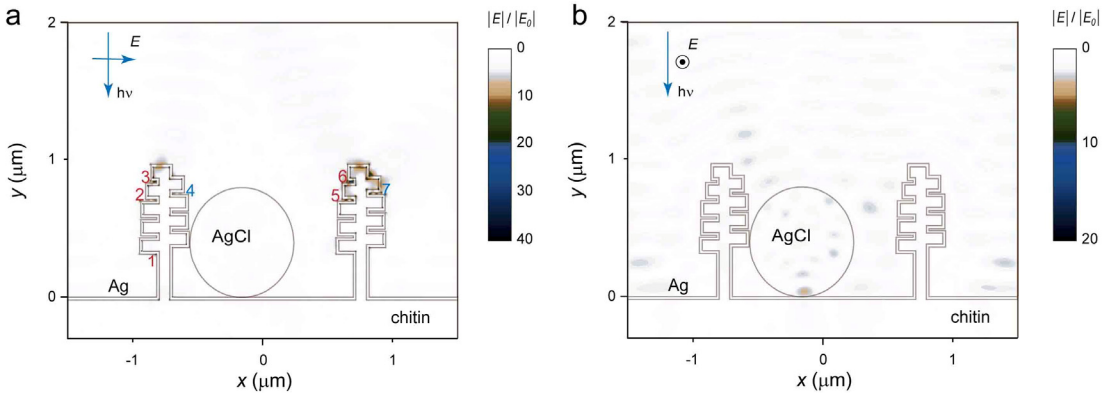

Figure S12. 2D FEM simulations (in water) of the EMF distribution on the 3D-Ag/AgCl excited by the 475 nm irradiation of (a) TM mode and (b) TE mode, respectively. The diameter of AgCl particle was set to be 800 nm. Here, the medium was water and normal irradiation of 475 nm was applied. Hotspots with EMF enhancement over 40-fold in intensity are marked with numbers in (a). Asymmetric spatial distribution of hotspots can be found.

Photoluminescence spectra of the Intact and As-Crushed 3D-Ag/AgCl (Figure S13).

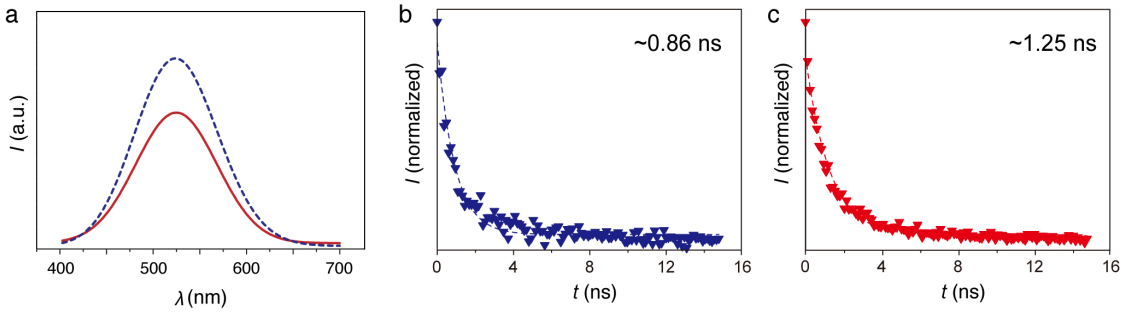

Figure S13. (a) Static and (b, c) transient PL spectra of intact (red line) and crushed (blue line) 3D-Ag/AgCl. The excitation wavelength was 395 nm.

Morphology of the As-Crushed 3D-Ag/AgCl (Figure S14).

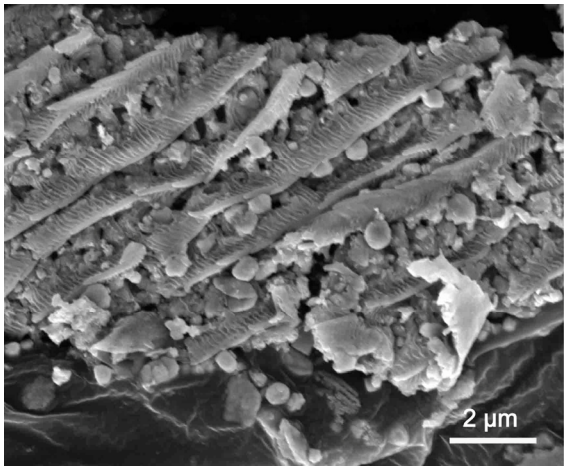

Figure S14. SEM image of the as-crushed 3D-Ag/AgCl.

XRD Results of 3D-Ag/AgCl (Figure S15).

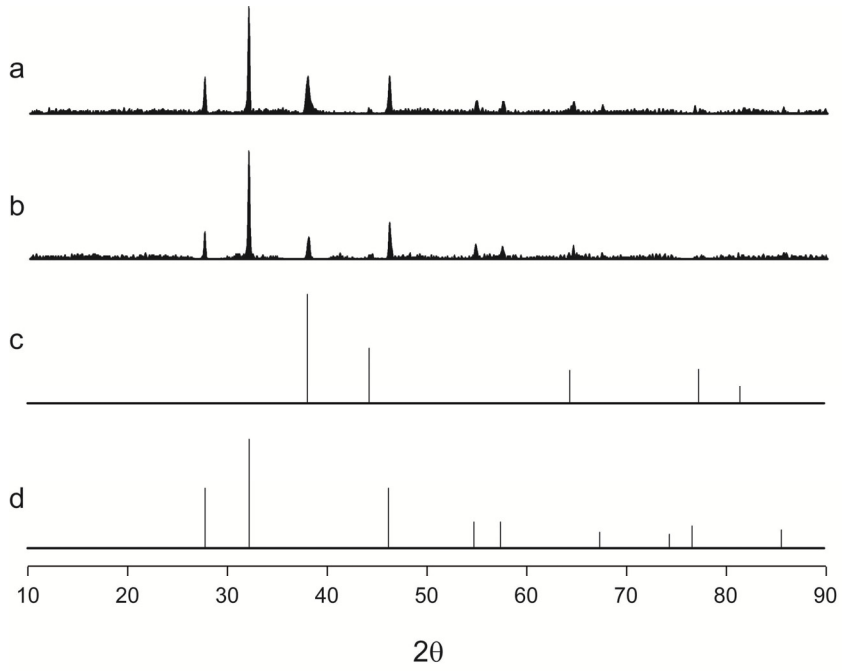

Figure S15. XRD results of (a) intact 3D-Ag/AgCl and (b) as-crushed 3D-Ag/AgCl. (c) and (d) show the diffraction data of Ag (JCPDS 65-2871) and AgCl (JCPDS 31-1238), respectively.

Effects of the Original Bio-Mass on the Water Splitting Processes (Figure S16).

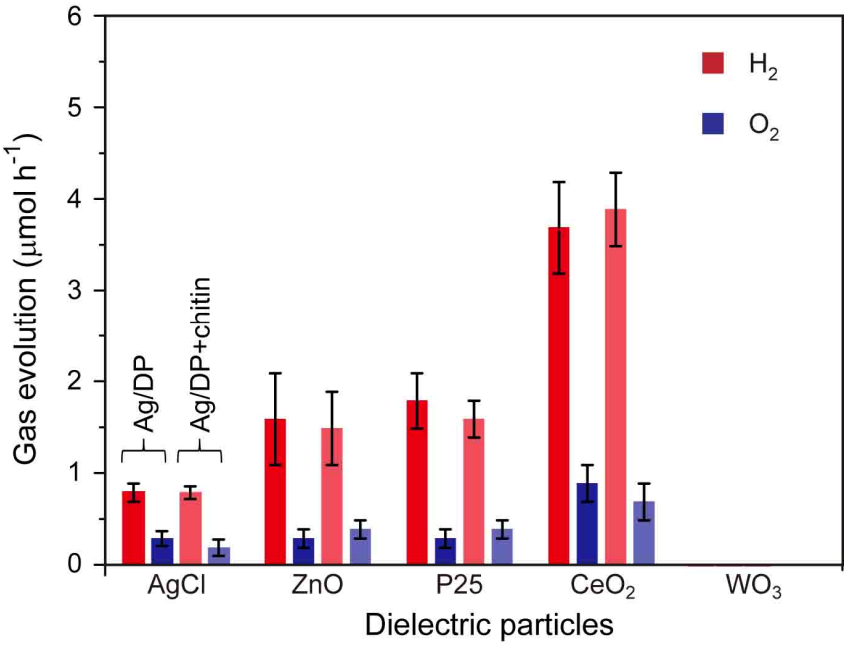

Figure S16. Effects of the original bio-mass (mainly chitin) on the water splitting properties for various systems.

Experimental Setup for the Water Splitting Measurements in Collision Mode (Figure S17).

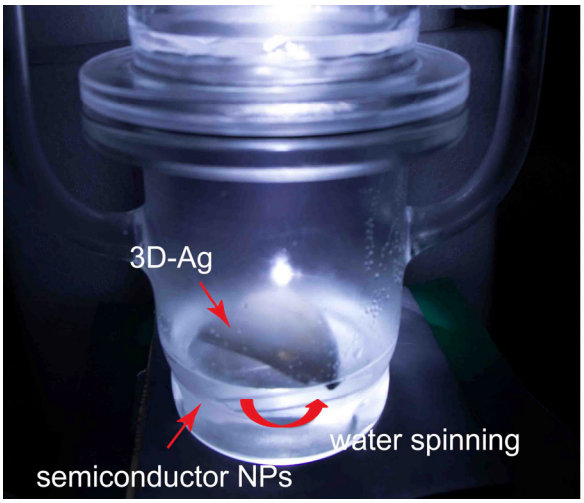

Figure S17. Experimental setup for the water splitting measurements in collision mode. Semiconductor nanoparticles (NPs) were suspended and stirred (100 rpm) in water during the measurements. The vessel was immersed in cooling water of 25 ºC during the water splitting process. The reaction temperature was thus kept at 28±2 ºC during the measurements.

Solar-Driven Overall Water Splitting on the 3D-Ag Combined with Various Commercial Dopant-Free Dielectric Particles (Figure S18).

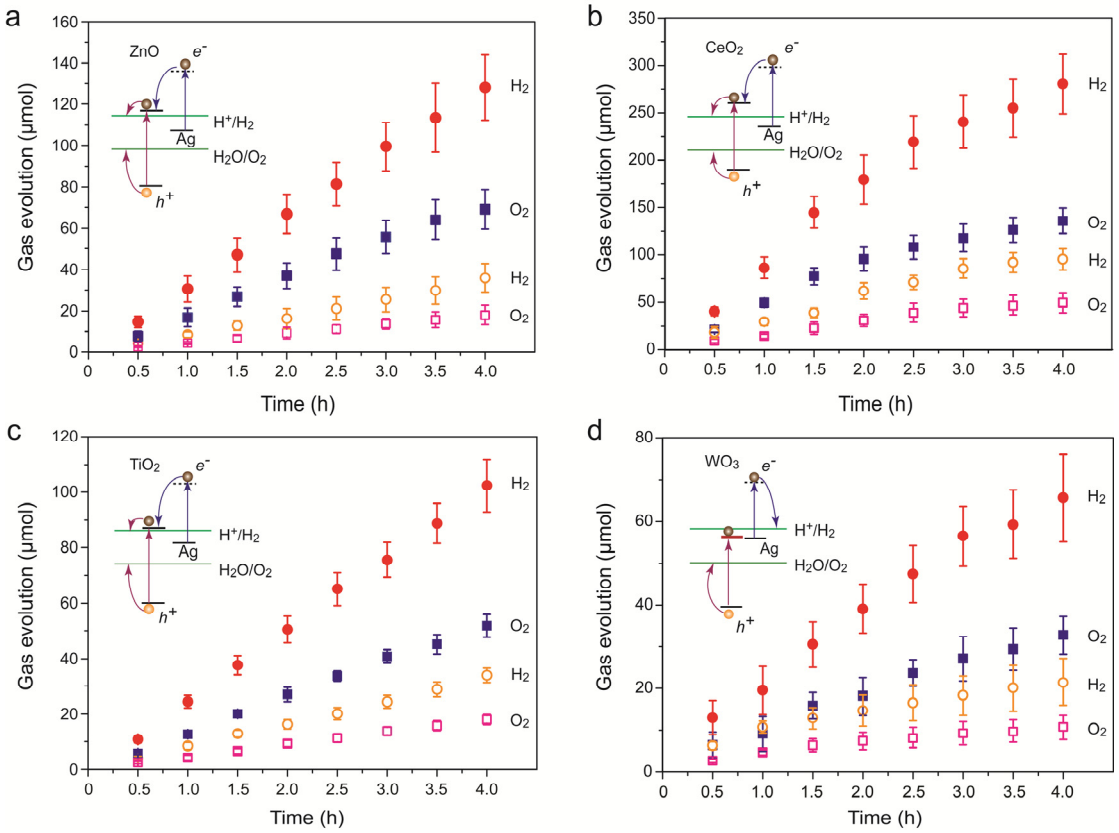

Figure S18. Gas evolution (collision mode) on (a) 3D-Ag/ZnO, (b) 3D-Ag/CeO_2, (c) 3D-Ag/P25, and (d) 3D-Ag/WO_3, respectively. Insets show the plausible carrier transfer processes. Filled and open symbols denote the intact and as-crushed Ag skeletons, respectively.

O_2 Evolution on Commercial WO_3 Using $AgNO_3$ as the Sacrificial Agent (Figure S19).

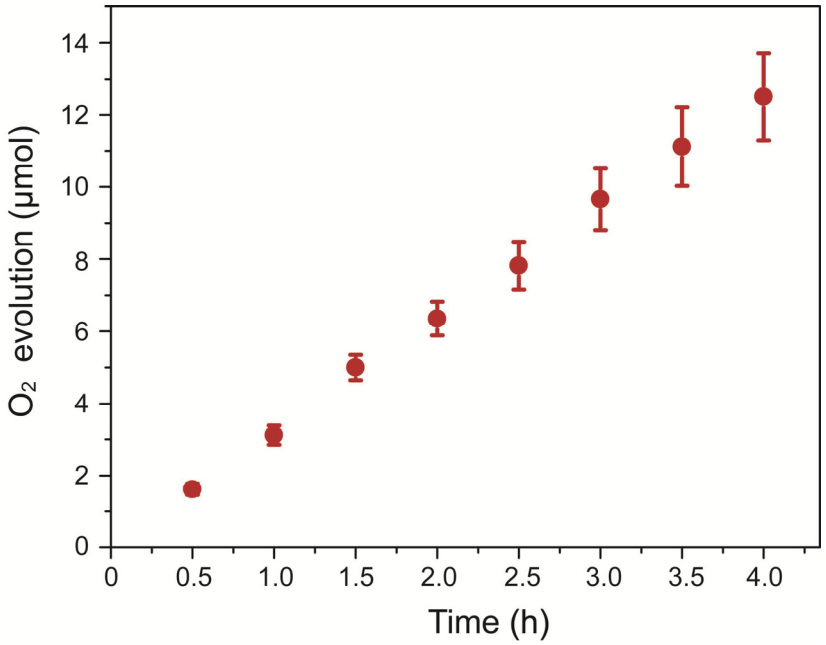

Figure S19. O_2 evolution on 100 mg of commercial WO_3 powder (T103856, Aladdin) suspended in a $AgNO_3$ water solution (0.01 M) as the sacrificial agent.

References

(1) Schafer, S.; Wang, Z.; Zierold, R.; Kipp, T.; Mews, A. Laser-Induced Charge Separation in CdSe Nanowires. *Nano Lett.* **2011**, *11*, 2672-2677.

(2) Liu, C. H.; Chang, Y. C.; Lee, S.; Zhang, Y. Z.; Zhang, Y. F.; Norris, T. B.; Zhong, Z. H. Ultrafast Lateral Photo-Dember Effect in Graphene Induced by Nonequilibrium Hot Carrier Dynamics. *Nano Lett.* **2015**, *15*, 4234-4239.

(3) Ashcroft, N. W.; Mermin, N. D. Solid State Physics (Holt, Rinehart and Winston, New York, 1976). **2005**.

(4) Cui, X. F.; Wang, C.; Argondizzo, A.; Garrett-Roe, S.; Gumhalter, B.; Petek, H. Transient Excitons at Metal Surfaces. *Nat. Phys.* **2014**, *10*, 505-509.

(5) Fujita, S.; Ho, H. C.; Okamura, Y. Quantum Theory of the Seebeck Coefficient in Metals. *Int. J. Mod. Phys. B* **2000**, *14*, 2231-2240.

(6) Vukusic, P.; Sambles, J. R. Photonic Structures in Biology. *Nature* **2003**, *424*, 852-855.